Elastic surrogate modeling of graphene nanoplatelet-reinforced epoxy using computational homogenization

Composites Science and Technology 256 (2024) 110761

Contents lists available at ScienceDirect

Composites Science and Technology

journal homepage: www.elsevier.com/locate/compscitech

Elastic surrogate modeling of graphene nanoplatelet-reinforced epoxy using computational homogenization

Ragnar Larsson [a,*], Danilo J. Carastan [b], Matheus M. de Oliveira [b], Linnéa Selegård [c], Mario Martínez [d]

[a] Division of Material and Computational Mechanics, Department of Industrial and Materials Science, Chalmers University of Technology, SE-412 96 Göteborg, Sweden
[b] Center for Engineering, Modeling and Applied Social Sciences, Universidade Federal do ABC, Santo André-SP, Brazil
[c] Saab AB, Linköping, Sweden
[d] Durability and Mechanical Integrity of Structural Materials Group, King Juan Carlos University, Móstoles, Spain

ARTICLE INFO

Keywords:
Surrogate model
Anisotropy
Computational homogenization
Composites
Graphene
Homogenization

ABSTRACT

2D nanoparticles, such as graphene or graphite nanoplatelets, are used as additives in polymer matrices to improve their stiffness and electrical conductivity. In this paper, a finite element-based model for homogenized macrolevel stiffness is developed to understand the increase in stiffness of the epoxy matrix induced by graphene nanoplatelets. The model uses image segmentation of regular SEM micrographs to account for the morphology of the graphene platelet network. Here, it is essential to include a fluctuation field in computational homogenization to describe microstructural relaxation. Platelets of the microstructure are modeled as embedded membranes, assuming perfect bonding to the polymer. To estimate the stiffness of the membrane, we used molecular dynamics simulations from a related paper on layered graphene platelets. A novel feature is the identified anisotropic and isotropic elastic surrogate models obtained by least-squares fits of homogenized microstructural responses. Surrogate models serve as a basis for the evaluation of the stiffness of the nanocomposites, and these models are validated through the Halpin–Tsai and Mori–Tanaka models. According to the experimental investigation, the results show that the samples exhibit an increase in stiffness of up to 10 % to 30 % for GNP contents ranging from 1 to 5 wt. %, respectively, obtained from the morphological properties and the weight fraction of the carbon filler.

1. Introduction

The use of carbon fiber reinforced polymers (CFRPs) is continually increasing in aeronautic applications in an attempt to reduce fuel consumption. The use of carbon fiber reinforced polymers (CFRPs) offers impressive weight savings potential for the aerospace industry, and many CFRP components are in regular commercial use. These components are typically based on composite laminates that suffer from inherent challenges, such as delamination and brittle behavior, related to their lack of through-thickness reinforcement. Graphene additives exhibit high thermal and electrical conductivity, excellent barrier properties, and extraordinarily high strength, enabling the development of multifunctional composites without adding significant weight to the components. Review articles [1,2] highlight the evolving field of graphene-related materials, in particular graphene-reinforced polymer-based composites with enhanced multifunctional properties. In earlier studies, inherently poor mechanical properties through the thickness of the laminate have been shown to be enhanced by aligned carbon nanotubes at the interfaces of the ply [3]. 2D nanostructures, such as graphite nanoplatelets (GNP), are now being explored as base resin additives in epoxy to improve these properties for CFRP. In particular, a significant increase in fracture toughness has been reported for GNP-enhanced unidirectional CFRP prepregs [4].

The mechanical response of graphene and related nanomaterials in polymer nanocomposites has been extensively investigated from the experimental perspective. For epoxy resins with well-dispersed and functionalized samples using graphene oxide (GO), the stiffening and strengthening effects are visible even at relatively low weight fractions <1 wt.% [5–7]. We also note the related increase in fracture toughness [8], while size effects are generally less pronounced in well-dispersed systems [9]. This is typically assigned to a good interaction between epoxy (as well as other thermoplastic matrices [6,10]) and the functional groups present in GO. A better interaction between

* Corresponding author.
E-mail address: ragnar@chalmers.se (R. Larsson).

https://doi.org/10.1016/j.compscitech.2024.110761
Received 31 January 2024; Received in revised form 5 June 2024; Accepted 14 July 2024
Available online 17 July 2024

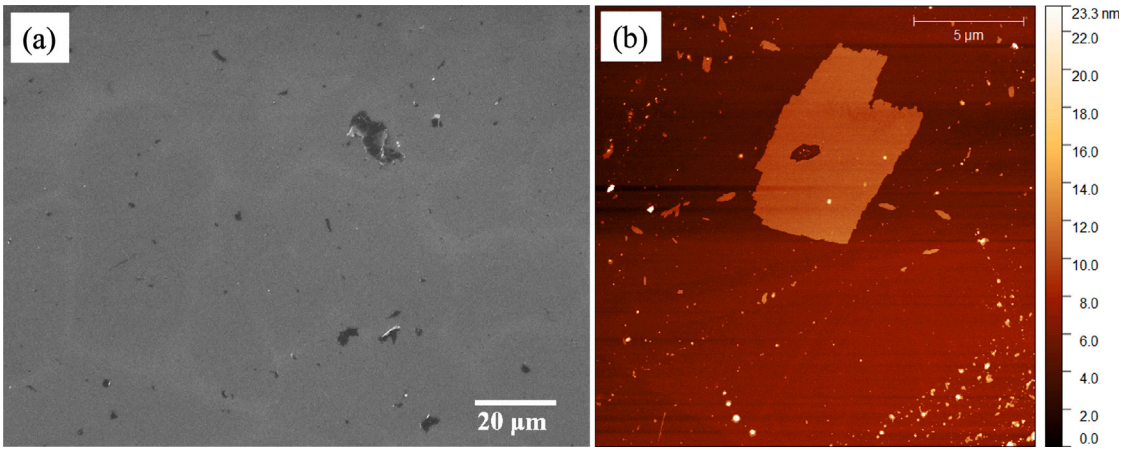

Fig. 1. SEM (a) and AFM (b) micrographs of representative GNP flakes.

nanoparticles and the matrix reduces the tendency to reagglomeration and naturally leads to better dispersion, while at the same time increasing the stiffening effect by improving the bonding with the polymer chains [11]. However, for GNP-epoxy systems, the interaction is weaker, leading to less pronounced stiffening and often harmful effects on tensile strength [12]; nevertheless, both an increase and a decrease in this property have been reported [10,13]. Furthermore, higher weight fractions tend to be considered for the GNP-epoxy system, typically 1–6 wt.%. For such large weight fractions, the increase in stiffness is more visible at the expense of a lower fracture toughness [10,13,14].

The addition of graphene-related materials to polymer resin requires optimized concentration and orientation to create material properties that meet the stiffness and strength requirements of these composites. For this, predictive modeling approaches are needed to assist in material design, both for effective matrix behavior at the microlevel and for the mesoscale of fiber-reinforced composites. The current mechanical analysis methods for these nanocomposites use analytical methods for the homogenization of the composite. Various approaches have been adopted in the literature based on the rule of the mixture, the Halpin–Tsai and Mori–Tanaka models, to estimate the effective elastic mechanical properties, for example [10,15]. More recently, Meng et al. [16] applied the Halpin–Tsai model for GNP-epoxy nanocomposites, noting discrepancies between predicted and experimental elastic modulus values due to the assumption of a perfectly random distribution of GNP flakes; however, surfactant modification improved accuracy by ensuring a more uniform dispersion in epoxy. Another recent article used finite element modeling of the micromechanics of a hybrid GNP-CNT-epoxy nanocomposite, emphasizing the effect of particle alignment on stiffness, in good correlation with predictions and experiments [17]. Haghighi et al. used multiscale modeling to determine the mechanical properties of GNP-CNT-epoxy nanocomposites. They used two distinct combinations of computational methods: molecular dynamics (MD) paired with finite element analysis, and MD combined with micromechanical modeling. Both approaches overpredicted the modulus improvements [18]. Difficulties arise with analytical homogenization as a result of the inherent planar nature of graphene and graphite nanoplatelet reinforcements. As can be seen in previous studies [13,19,20], the stiffness tends to be over- or underestimated depending on the application of the Halpin–Tsai or Mori–Tanaka methods. Various approaches are proposed to adjust for the shape of platelet filler, for example [13,21]. In the method presented by Young et al. [22] an effective modulus is formulated in the reinforcement plane of graphene nanoplatelets using shear lag theory for shear stress transfer between the constituent surfaces [23]. Multiscale computational approaches have also been considered at the molecular level [14] based on MD modeling and continuum mechanics based on the microlevel [24].

In this paper, we exploit the formulations presented in [24] based on computational homogenization [25,26] for the effective elastic properties of epoxy composites enhanced with GNP with various weight fractions of the content of carbon nanoparticles. Dirichlet and periodic boundary conditions in the weak sense [27] are used to describe the crucial fluctuation of displacement in the microstructure. 2D-GNP enhancements in the composite are treated as membranes embedded in the bulk polymer [28]. These membranes have their own mechanical balance relationship, which adds a stiffening membrane effect to the composite. The properties of neat epoxy are taken from standard tensile tests and a data sheet, while molecular dynamics simulations presented in [14] of the layered graphene elements are used to estimate the stiffness of the membrane. A representative area element (RAE) of the reinforced polymer matrix is established on the basis of regular SEM micrographs of the graphene nanoplatelet network. Unlike X-ray computed tomography image data that identify 2D phases as volumes [29], micrographs are used here to segment virtual representations of the microstructure morphology in terms of the polymer matrix and the membranes that represent the GNP network. A special duplication-based segmentation procedure is developed to fit the microstructure to the (given) weight fraction of the GNP. From the homogenization analysis, the macroscopic stiffness properties are simulated in relation to the isotropic elastic and anisotropic surrogate models fitted with least squares. Compared with experimental results, it is necessary to include a finite element-represented fluctuation field in computational homogenization to describe proper microstructural relaxation. The results show that the samples exhibit an improved stiffness of up to 10%–30% due to the morphological properties and the weight fraction of the GNP content. The anisotropic surrogate model reveals a significant local variation of the stiffness parameters for increasing volume concentrations and for different orientations and distributions of the graphene. Estimates are generally slightly higher than those for experimental tensile testing.

2. Materials and methods

2.1. Experimental development of graphene–epoxy composites

Epoxy-GNP nanoplatelet composites were prepared to serve as a model system to validate the stiffness homogenization model developed herein. A two-component aeronautical grade epoxy system (Araldite LY 5052/Aradur 5052) was used as the matrix. The graphene nanoplatelets used were exfoliated graphene/graphite nanoplatelets supplied by 2D fab, without any modification. The flakes have an average thickness of 5.57 ± 0.50 nm, as measured by atomic force microscopy (AFM, Brucker Dimension Icon, Massachusetts, USA), which is equivalent to approximately 17 layers [30]. The average lateral size is 0.88 ±

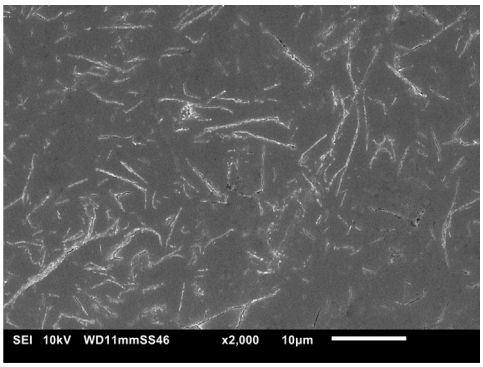

(a) SEM image of a 5 wt % graphene-epoxy nanocomposite.

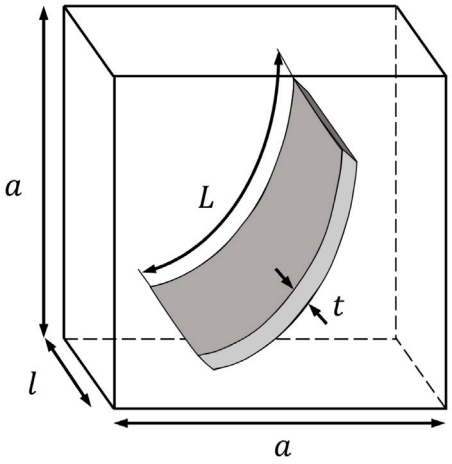

(b) Schematic of enhanced polymer by GNP in a region with volume $V = l\,a^2$, where l is the average depth of the GNP particles. The GNP volume fraction v^g based on the number of visible GNPs, whose average thickness is t on the surface in Fig. 2a.

Fig. 2. GNP volume fraction based on surface image analysis.

0.38 μm, measured by scanning electron microscopy (SEM, Jeol JCM-6000 Plus, Tokyo, Japan) micrographs (Fig. 1). A suitable amount of graphene nanoplatelets was first manually mixed with the liquid resin in a beaker, and then the system was sonicated for 120 min in a 70 W 40 kHz ultrasonic bath (Sanders SoniClean 2PS, Minas Gerais, Brazil), with manual stirring every 40 min to maintain homogeneity. The acoustic power delivered to the samples was measured using the calorimetric method [31] and was found to be ≈ 0.53 W. Previous studies have shown that this dispersion method is able to disperse the GNP flakes whilst maintaining their electrical and mechanical properties [32]. After the addition of hardener, the mixture was poured into the appropriate silicone molds, cured at 25 °C for 24 h, and post-cured at 100 °C for 4 h. The weight fraction of the graphene nanoplatelets in the cured composite was 1, 3 and 5 wt.%. It is important to note that the addition of GNP to the resin substantially increases its viscosity, which may pose challenges in achieving a completely uniform mixture.

Scanning electron microscopy images of the cross section of the composites were used as input for the finite element analysis. The composite sample was initially cut with an Isomet cutter (Buehler, Illiois, USA), and the exposed surface was sanded and polished with nanosilica as the polishing medium. The sample was sputter coated with a 15 nm thick gold layer, and microscopic observations were made on the SEM with a voltage of 10 kV and a secondary electron detector.

2.2. Experimental tensile testing of the graphene–epoxy composites

Experimental tensile tests were carried out using an Instron universal testing machine (Massachusetts, USA) equipped with a 50 kN load cell, following the ISO 527 standard guidelines. Dumbbell-shaped specimens of 1BA type were prepared and the tests were carried out at room temperature with a crosshead displacement rate of 1 mm min^{-1}, corresponding to a strain rate of 6.67×10^{-4} s^{-1}. Five specimens for each condition were tested and the results were averaged.

2.3. Image segmentation of GNP enhanced epoxy composite

Microscopic images of the GNP-epoxy composites collected experimentally were then used to create virtual representations of the microstructure of the experimental material. Fig. 2(a) shows sections of graphene nanoplatelets that appear as light gray lines, showing the 2D morphology of GNPs in the composite in terms of different lengths and

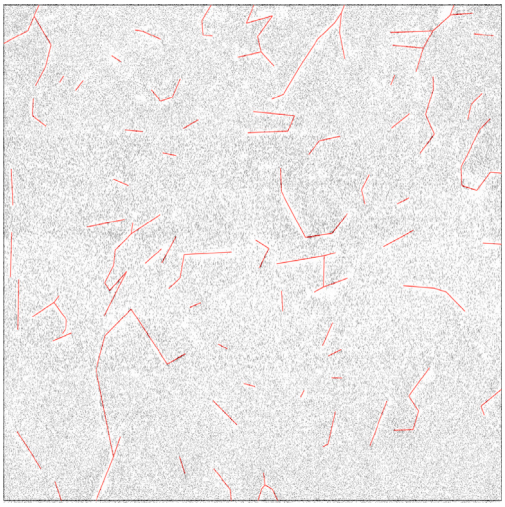

Fig. 3. Digitized microstructure (red lines) over micrograph for a 3 wt.% GNP content.

thicknesses of GNPs in the darker epoxy matrix. Micrographs such as the one in Fig. 2(a) were segmented using the Digitizer tool available in the Origin graphing software (OriginLab Corporation, Northampton, USA). The image segmentation process was carried out by picking the coordinates of each beginning and end of the observed GNPs to digitize the micrograph, approximating the visible GNP morphology as lines between the beginning and end points. Aggregates of GNPs or non-straight GNP morphologies have been approximated, discretizing them into several lines (polyline). In segmentation, GNPs are assumed to be membranes, identified through digitized polylines, embedded in the polymer matrix. An example of a segmented microstructure is shown in Fig. 3. It is emphasized that only the surface of the sample in Fig. 2(a) is visible by SEM; in this case, with the internal surface of the GNP-epoxy composite of 3 wt%.

Because only a portion of the GNPs is visible from the SEM, it is necessary to combine the segmentation with the volume and weight fractions of the GNP filler from the processing of the composite. To this end, it is assumed that GNPs are randomly distributed on the surface and in the volume of the statistically representative cube with the total

volume V as in Fig. 2(b). The schematic in Fig. 2(b) shows the enhanced polymer by GNP, where the total volume of GNP can be represented by $V^g = l\,t\int_0^{L_t} ds$. Note that L_t is the *total* length of the dimension in the plane of the 2D GNP elements, while l is the depth of the GNP elements. With the average thickness t for all GNPs, the volume fraction is

$$v^g = \frac{V^g}{V} = \frac{L_t\,t}{a^2} = n_d\frac{L\,t}{a^2} \text{ with } L = \sum_{i=1}^{n}\int_{I_i} ds \tag{1}$$

where L is the *visible* length of the GNPs from the SEM-analysis taken as the sum of all sub-lengths of the GNP intervals I_i of the digitized microstructure in Fig. 3. In (1) we also introduced the number of duplicated 2D morphologies n_d that are required to preserve the given volume fraction of GNP from nanocomposite processing. Therefore, we emphasize that n_d is not the number of layers of GNP-flakes; it is considered a representative value of the invisible flake morphology from the 2D SEM analysis. Furthermore, the intrinsic densities of the GNP and matrix are ρ_g and ρ_m, respectively, so that the weight fraction w^g of GNPs is

$$w^g = \frac{\rho_g v^g}{\rho_m(1-v^g)+\rho_g v^g} \Rightarrow v^g = \frac{\rho_m w^g}{\rho_m w^g + \rho_g(1-w^g)} \tag{2}$$

Upon combining (1) and (2) we finally arrive at

$$n_d = \frac{a^2}{L\,t}\frac{w^g\rho_m}{(1-w^g)\rho_g + w^g\rho_m} \tag{3}$$

3. Computational homogenization and elastic surrogate modeling of the nanocomposite

3.1. Homogenization procedure

To predict the increase in the stiffness of the nanocomposite, a finite element-based homogenization procedure has been developed. In this method, the effective elastic representation of the 2D nanoplatelet-enhanced epoxy composite is homogenized using computational homogenization, where the 2D GNPs are modeled as membrane reinforcements embedded in the neat epoxy [28]. For homogenization, embedded GNPs are resolved using the image analysis method presented in Section 2.3. Only a portion of the GNPs are visible from the SEM; however, we let the orientation and discrete locations in $\Omega_\square$ of the GNP elements obtained from the surface images represent the morphology of the nanostructure. Taking into account a GNP element in the schematic Fig. 4b, the natural coordinate s runs along the material points $\boldsymbol{x}[s]$ of the GNP membranes. The tangent vector is $\boldsymbol{n} = \boldsymbol{x}'[s]$. As alluded to in Fig. 4b, the dimension of the GNP elements in the depth dimension is l. The GNP stress response is governed by the normal force of the membrane N. In terms of interaction with the polymer, full GNP-polymer bonding is assumed.

The planar region $\Omega_\square$ is assumed to be a plane strain sheet with thickness l as shown in Fig. 4. In the present context with embedded membranes in the polymer matrix, the Hill–Mandel condition [26] yields the virtual work equivalence between macroscopic and microscopic fields as

$$A\,\bar{\boldsymbol{\sigma}} : \delta\bar{\boldsymbol{\epsilon}} = \int_{\Omega_\square}\boldsymbol{\sigma}[\boldsymbol{\epsilon}] : \delta\boldsymbol{\epsilon}\,d\Omega + \int_L N[\epsilon]\delta\epsilon\,ds\ \forall\delta\boldsymbol{\epsilon} \tag{4}$$

where $A = a^2$ is the area of the square region $\Omega_\square$. As mentioned, it is assumed that the normal strain of the GNP membranes is affine with the strain of the polymer, so that $\epsilon = (\boldsymbol{n}\otimes\boldsymbol{n}) : \boldsymbol{\epsilon}$. Furthermore, in (4) an overbar denotes quantities at the macrolevel, whereby $\bar{\boldsymbol{\sigma}}$ is the homogenized macrostress and $\delta\bar{\boldsymbol{\epsilon}}$ is the virtual strain at the macrolevel. At the microlevel, $\boldsymbol{\sigma}$ is the polymer stress, N [N/m] is the *normal membrane force* of the resolved GNPs and $\boldsymbol{\epsilon}$ is the engineering strain.

To link macro- and micro-stress responses, the strain at the microlevel $\boldsymbol{\epsilon}$ is subdivided into terms of a subscale strain $\boldsymbol{\epsilon}^s$ defined as $\boldsymbol{\epsilon} = \bar{\boldsymbol{\epsilon}} + \boldsymbol{\epsilon}[\boldsymbol{u}^s]$, where $\boldsymbol{u}^s$ is the subscale displacement field. Also, note that $\bar{\boldsymbol{\epsilon}}$ is the given *macroscopic* strain and $\boldsymbol{u}^s$ is the subscale displacement field resolved by FE from the balance relation (6) below. The corresponding homogenized macrostress of the GNP enhanced polymer is then obtained as

$$\bar{\boldsymbol{\sigma}} = \bar{\boldsymbol{\sigma}}^{\mathrm{m}} + \bar{\boldsymbol{\sigma}}^{\mathrm{GNP}} \text{ with } \bar{\boldsymbol{\sigma}}^{\mathrm{m}} = \frac{1}{A}\int_{\Omega_\square}\boldsymbol{\sigma}\,d\Omega \text{ and } \bar{\boldsymbol{\sigma}}^{\mathrm{GNP}} = \frac{1}{A}\sum_{i=1}^{n}\int_{I_i} N\boldsymbol{n}\otimes\boldsymbol{n}\,ds \tag{5}$$

where n is the number of visible GNPs of the RAE. The second part $\bar{\boldsymbol{\sigma}}^{\mathrm{GNP}}$ of macrostress represents the additional contribution due to the membrane action of the embedded GNPs. This results from the virtual work done by the microstructure in the RAE considering the full interaction between the embedded GNP-membranes and the matrix. The structure tensor $\boldsymbol{n}\otimes\boldsymbol{n}$ specifies the orientation of the membrane action. We emphasize that the membrane force N (with unit N/m) is a different quantity compared to the stress, while the homogenized membrane stress $\bar{\boldsymbol{\sigma}}^{\mathrm{GNP}}$ has unit MPa.

Fundamental to the homogenized response in (5) is that the microstress $\boldsymbol{\sigma}[\boldsymbol{\epsilon}]$ and membrane force $N[\epsilon]$ fields are self-balancing in the sense that

$$\begin{aligned}\int_{\Omega_\square}\boldsymbol{\sigma} : \boldsymbol{\epsilon}\left[\delta\boldsymbol{u}^s\right]dA + \sum_{i=1}^{n}\int_{I_i} N[\epsilon]\delta\epsilon\,ds \\ = \int_{\Gamma_{\square m}}\left(\boldsymbol{t}\cdot\delta[\![\boldsymbol{u}^s]\!]_m + \delta\boldsymbol{t}\cdot[\![\boldsymbol{u}^s]\!]_m\right)ds\ \forall\,\delta\boldsymbol{u}^s,\,\delta\boldsymbol{t}\end{aligned} \tag{6}$$

corresponding to the separate static equilibrium statements for the bulk and for the GNP-elements within the RAE

$$\boldsymbol{\sigma}\cdot\boldsymbol{\nabla} = \boldsymbol{0}\ \forall\boldsymbol{x}\ \in\Omega_\square \tag{7a}$$

$$\frac{dN}{ds} = 0\ \forall\boldsymbol{x}[s]\ \in I_{i=1,\ldots,n} \tag{7b}$$

where $\boldsymbol{\nabla}$ is the gradient operator. In (6), full bonding is assumed for all GNPs, which is $\epsilon = (\boldsymbol{n}\otimes\boldsymbol{n}) : \boldsymbol{\epsilon}[\boldsymbol{u}^s]$. To allow periodic boundary conditions (PBC), the tractions are $\boldsymbol{t}_m + \boldsymbol{t}_b = \boldsymbol{0}$ and the subscale displacements are $\boldsymbol{u}^s_m - \boldsymbol{u}^s_b = \boldsymbol{0}$ on the master (subindex m) and backsides (subindex b) of the RAE boundaries, as shown in Fig. 4a. As an extension of [24], this is formulated in a weak sense in (6) where we used the notation $[\![\boldsymbol{u}^s]\!]_m = \boldsymbol{u}^s_m - \boldsymbol{u}^s_b$. More details are found in [27]. In the case of weak Dirichlet boundary conditions (DBC), we simply let $[\![\boldsymbol{u}^s]\!]_m \to \boldsymbol{u}^s$ along the entire $\Gamma_\square$ of the RAE.

The balance relation (6) is solved using finite elements, approximating the subscale field $\boldsymbol{u}^s[\boldsymbol{x}]$ so that the bulk polymer is discretized using standard 2D bilinear elements and the membrane structures are considered consistent with the bulk polymer elements. Moreover, piecewise constant tractions $\boldsymbol{t}$ are considered along $\Gamma_{\square m}$. The membranes are embedded within the common face between two adjacent bulk FE elements. Here, elastic response of the bulk and the membranes is assumed so that

$$\boldsymbol{\sigma} = \boldsymbol{E}_m : \left(\bar{\boldsymbol{\epsilon}} + \boldsymbol{\epsilon}\left[\boldsymbol{u}^s\right]\right) \text{ with } \boldsymbol{E}_m = 2G_m\boldsymbol{I}_d + K_m\boldsymbol{1}\otimes\boldsymbol{1} \tag{8a}$$

$$N := n_d\,E^f\,(\bar{\epsilon} + \epsilon[\boldsymbol{u}^s]) \tag{8b}$$

where G_m and K_m are the elastic shear and bulk moduli for the isotropic neat epoxy. We also introduce the fourth-order deviatoric projection operator $\boldsymbol{I}_d$ in terms of the fourth-order $\boldsymbol{I}$ and second-order identity tensor $\boldsymbol{1}$ defined by $\boldsymbol{I}_d = \boldsymbol{I} - \frac{1}{3}\boldsymbol{1}\otimes\boldsymbol{1}$. The fourth order projection operator projects any second-order tensor onto its deviatoric part; for example, the strain deviator is $\boldsymbol{\epsilon}_d = \boldsymbol{I}_d : \boldsymbol{\epsilon} = \boldsymbol{\epsilon} - \frac{1}{3}\epsilon_v\boldsymbol{1}$. Further elaboration on this definition can be found in a prior publication [33]. Furthermore, in (8b), E^f is the stiffness of the GNP membrane. The membrane stiffness appears to depend on the number of layers of GNP particles, as discussed in Section 4.

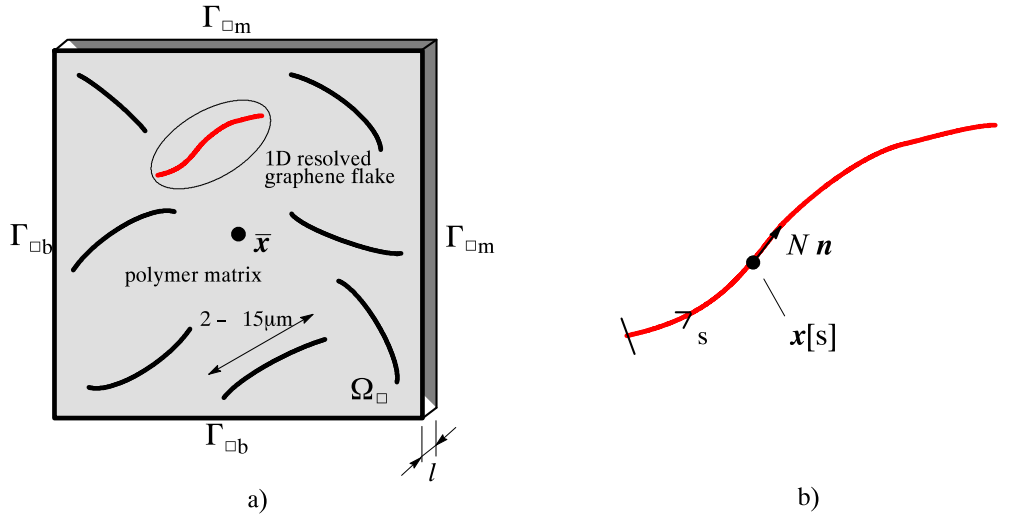

Fig. 4. Representative area element, with side length a, of GNP elements embedded in neat epoxy. (a) Principal 2D image of GNPs embedded in the polymer matrix in the RAE region $\Omega_{\square}$. To handle periodic boundary conditions, the boundary consists of master boundaries $\Gamma_{\square m}$ (on top and to the "right") alongside back boundaries $\Gamma_{\square b}$. (b) Close-up of GNP considered as a membrane with material points $\boldsymbol{x}[s]$ in terms of natural coordinates along the interval I. The unit tangent vector of the membrane is $\boldsymbol{n} = \boldsymbol{x}'[s]$.

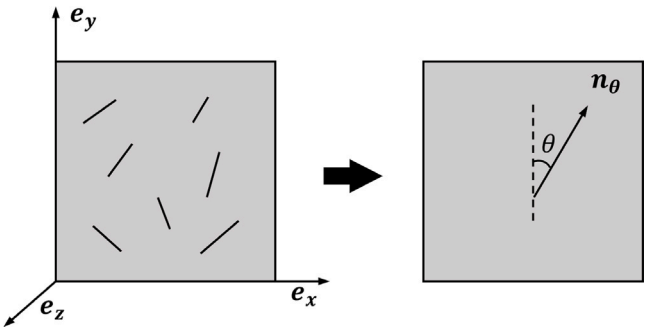

Fig. 5. Schematic of the equivalent transverse isotropic elastic representation of the computationally homogenized nanoplatelet-reinforced composite. The preferred orientation is $\boldsymbol{n}_\theta$.

3.2. Transverse isotropic elastic surrogate model

To investigate the stiffness variation in the composite as induced by the morphology of the SEM images, a surrogate transverse isotropic elastic model is introduced. The homogenized composite is assumed to have a preferred orientation $\boldsymbol{n}_\theta$ that rotates an angle θ with respect to the vertical y axis of the RAE, as shown in Fig. 5. We emphasize that the investigation concerns the degree of elastic anisotropy and that there is no connection to any other physical orientation of the sample.

The elastic stiffness is established from three independent deformations applied to the RAE, whereby we obtain the elastic stiffness for the planar case in Voigt form as

$$\underline{\overline{\boldsymbol{E}}} = \begin{pmatrix} \bar{\sigma}_x^1 & \bar{\sigma}_x^2 & \bar{\sigma}_x^3 \\ \bar{\sigma}_y^1 & \bar{\sigma}_y^2 & \bar{\sigma}_y^3 \\ \bar{\tau}_{\mathrm{xy}}^1 & \bar{\tau}_{\mathrm{xy}}^2 & \bar{\tau}_{\mathrm{xy}}^3 \end{pmatrix} \tag{9}$$

Here, each column is the homogenized stress response $\{\underline{\bar{\boldsymbol{\sigma}}}^i = (\bar{\sigma}_x, \bar{\sigma}_y, \bar{\tau}_{xy})\}_{i=1,2,3}$ of the triad of unit deformations $\left\{\underline{\bar{\boldsymbol{\epsilon}}}^i = \left(\bar{\epsilon}_x, \bar{\epsilon}_y, \bar{\gamma}_{\mathrm{xy}}\right)\right\}_{i=1,2,3}$ defined as

$$\left\{\bar{\epsilon}_x = 1, \bar{\epsilon}_y = 0, \bar{\gamma}_{\mathrm{xy}} = 0\right\}_{i=1}, \ \left\{\bar{\epsilon}_x = 0, \bar{\epsilon}_y = 1, \bar{\gamma}_{\mathrm{xy}} = 0\right\}_{i=2}, \\ \left\{\bar{\epsilon}_x = 0, \bar{\epsilon}_y = 0, \bar{\gamma}_{\mathrm{xy}} = 1\right\}_{i=3} \tag{10}$$

Following the developments in [33], transverse elastic isotropy may be represented in tensor form as

$$\boldsymbol{E} = 2G\boldsymbol{I}_d + 2G_s\boldsymbol{I}_s + K\boldsymbol{1}\otimes\boldsymbol{1} + E\boldsymbol{m}_\theta\otimes\boldsymbol{m}_\theta \text{ with } \boldsymbol{m}_\theta = \boldsymbol{n}_\theta\otimes\boldsymbol{n}_\theta \tag{11}$$

The fourth order shear tensor $\boldsymbol{I}_s$ projects an arbitrary strain into pure shear associated with $\boldsymbol{n}_\theta$ defined as

$$\boldsymbol{I}_s = \frac{1}{2}\left(\boldsymbol{1}\bar{\otimes}\boldsymbol{m}_\theta + \boldsymbol{m}_\theta\bar{\otimes}\boldsymbol{1}\right) - \boldsymbol{m}_\theta\otimes\boldsymbol{m}_\theta \tag{12}$$

In (11), G and K are the isotropic shear and bulk moduli for the nanocomposite, while the anisotropy parameters G_s and E are the contributions of shear and normal stiffness associated with the preferred orientation $\boldsymbol{n}_\theta$ induced by the platelet mixture. It appears that the elastic parameters $\{G, G_s, K, E\}$ are related to the classical parameters of elastic transverse isotropy $\{E_1, E_2, G_{23}, G_{12}, \nu_{12}\}$ ("1" denotes the longitudinal "fiber" direction), cf. [33], as

$$E_2 = \frac{4G(E(G+3K)+9GK)}{E(4G+3K)+4G(G+3K)}, \ G_{23} = G, \\ E_1 = E + \frac{9GK}{G+3K}, \ G_{12} = G + \frac{G_s}{2}, \ \nu_{12} = \frac{9K}{2(G+3K)} - 1 \tag{13}$$

Here, the sensitivity to the orientation of the "fiber" (or anisotropy) is reflected in the ratio E_1/E_2. Note that the ratio $E_1/E_2 \to 1$ as the "fiber" stiffness $E \to 0$ and the shear stiffness $G_{12} \to G$ when $G_s \to 0$. Furthermore, to obtain the equivalent transverse isotropic elastic representation of the computationally homogenized nanoplatelet reinforced composite in (9), a least squares fit is defined from the minimization problem

$$\{G, G_s, K, E, \theta\} = \arg\left(\min\left|\underline{\overline{\boldsymbol{E}}} - \underline{\boldsymbol{E}}\right|^2\right) \rightsquigarrow \{E_2, G_{23}, E_1, G_{12}, \nu_{12}, \theta\} \tag{14}$$

where $\underline{\boldsymbol{E}}$ is the Voigt matrix representation of the tensor in (11). The output from the least-squares fit includes the parameters $\{G, G_s, K, E, \theta\}$, which define the macrolevel stiffness $\underline{\boldsymbol{E}}$, leading to the classical transverse anisotropy parameters in (13). Note that the orientation vector of the preferred GNP orientation vector $\boldsymbol{n}_\theta$ is identified from the orientation angle θ in the planar case as $\boldsymbol{n}_\theta = \{\sin\theta, \cos\theta, 0\}$, cf. Fig. 5. In practice, it turns out to be very difficult to evaluate the best fit with respect to angle θ. Instead, a search algorithm was adopted, varying the angle in the range $0 \le \theta \le 180°$, to obtain the global minimum in (14). As alluded to in (14), we make use of (13) to convert the identified model parameters to the corresponding classical ones.

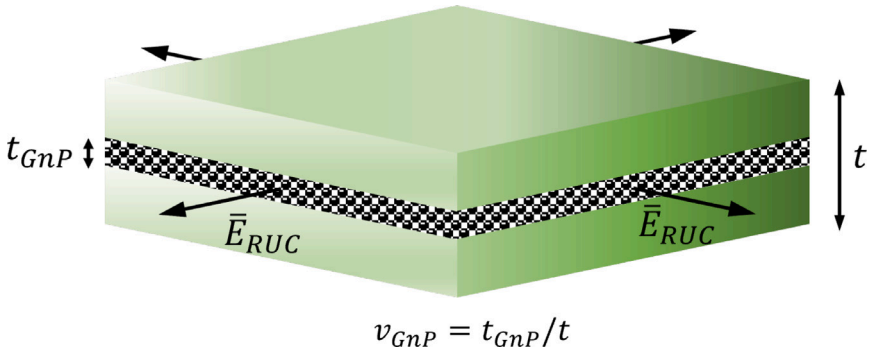

Fig. 6. Schematic figure of an RUC for MD simulation of the homogenized lateral stiffness modulus $\bar{E}_{RUC}$ and volume fraction v^{GNP} considered in [14].

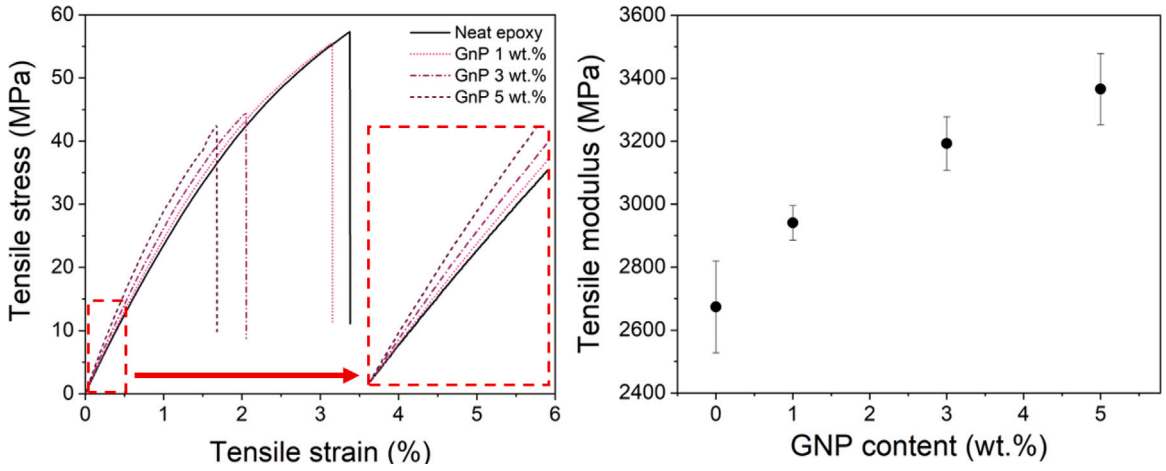

Fig. 7. Tensile test curves for neat epoxy and GNP-reinforced nanocomposites (left); averaged elastic modulus as a function of GNP weight content (right).

3.3. Isotropic elastic surrogate model

We also consider isotropic elasticity to act as a surrogate model for the homogenized response of the nanocomposite. Then it is assumed from the outset that there is no preferred orientation of the stiffness properties. This property is anticipated for well-dispersed specimens in processing, although local anisotropy may be present without affecting the overall behavior at the macrolevel. The procedure is completely analogous to the one described in 3.2 for the assumed anisotropic response, where the isotropic elasticity stiffness tensor is defined as

$$\boldsymbol{E} = 2G_{iso}\,\boldsymbol{I}_d + K_{iso}\,\mathbf{1}\otimes\mathbf{1} \tag{15}$$

The minimization problem for the best fit is then redefined for the isotropic elasticity parameters $\{K_{iso}, G_{iso}\}$ as

$$\{K_{iso}, G_{iso}\} = \arg\left(\min\left|\overline{\underline{E}} - \underline{E}\right|^2\right) \rightsquigarrow \{E_{iso}, \nu_{iso}\} \tag{16}$$

The elastic constants $\{E_{iso}, \nu_{iso}\}$ are related to the output fitting parameters from (16) through

$$E_{iso} = \frac{9K_{iso}G_{iso}}{3K_{iso}+G_{iso}}\,,\ \nu_{iso} = \frac{E_{iso}}{2G_{iso}} - 1 \tag{17}$$

4. Experimental results and data preparation

To estimate the stiffness of the GNP membrane E^f in (8b) the results of [14] on the GNP-reinforcement of epoxy are exploited. Here, the homogenized stiffness modulus in the lateral direction $\bar{E}_{RUC}$ is obtained from MD simulations of a representative unit cell (RUC) as in Fig. 6. Different results are reported for a number of polymer-graphene functionalized layers. Upon assuming the rule of mixtures for the 1D lateral response of the RUC, we find that the contribution of the intrinsic graphene stiffness is

$$E_g = \frac{\bar{E}_{RUC} - (1-v^{GNP})E_m}{v^{GNP}} \text{ with } v^{GNP} = \frac{t}{t_{GNP}} \tag{18}$$

where v^{GNP} is the volume fraction GNP in the RUC and $\bar{E}_{RUC}$ is the homogenized lateral stiffness from the MD-simulations in ref [14]. Here, the stiffness contribution of the polymer is included, even when it is relatively small. From the data in [14] for v^{GNP} and $\bar{E}_{RUC}$ based on the cross-link density of the polymer 80%, we find that the intrinsic stiffness is fairly insensitive to the number of layers. The average value is $E_g \approx 876 \cdot 10^3$ MPa, taking into account the stiffness of the matrix E_m =2674 MPa. The stiffness of the GNP membrane in the RAE representation (8b) is then $E^f = n_l\, t_g\, E_g$, with t_g = 3.4 Å as shown in Table 1. Here, it can be observed that E^f (with $n_l = 1$) is slightly reduced compared to the experimentally determined values of the linear part of a graphene monolayer [34].

Table 1
Material parameters for elastic isotropy of the neat epoxy and mechanical properties of a GNP layer.

E_m MPa	ν_m –	G_m MPa	K_m MPa	$E^f = n_l\, t_g\, E_g$ N/m
2674	0.36	983	3183	$297.82\, n_l$

The neat epoxy was tested as specified in Section 2.2. The results are shown in Fig. 7, where the linear regime is used to obtain the modulus of elasticity. The Poisson ratio is $\nu_m = 0.36$, which leads to the elastic isotropy properties in (8a) of the epoxy. The corresponding shear and bulk stiffnesses are shown in Table 1. Tensile tests of nanocomposite samples were performed for the different weight fractions considered.

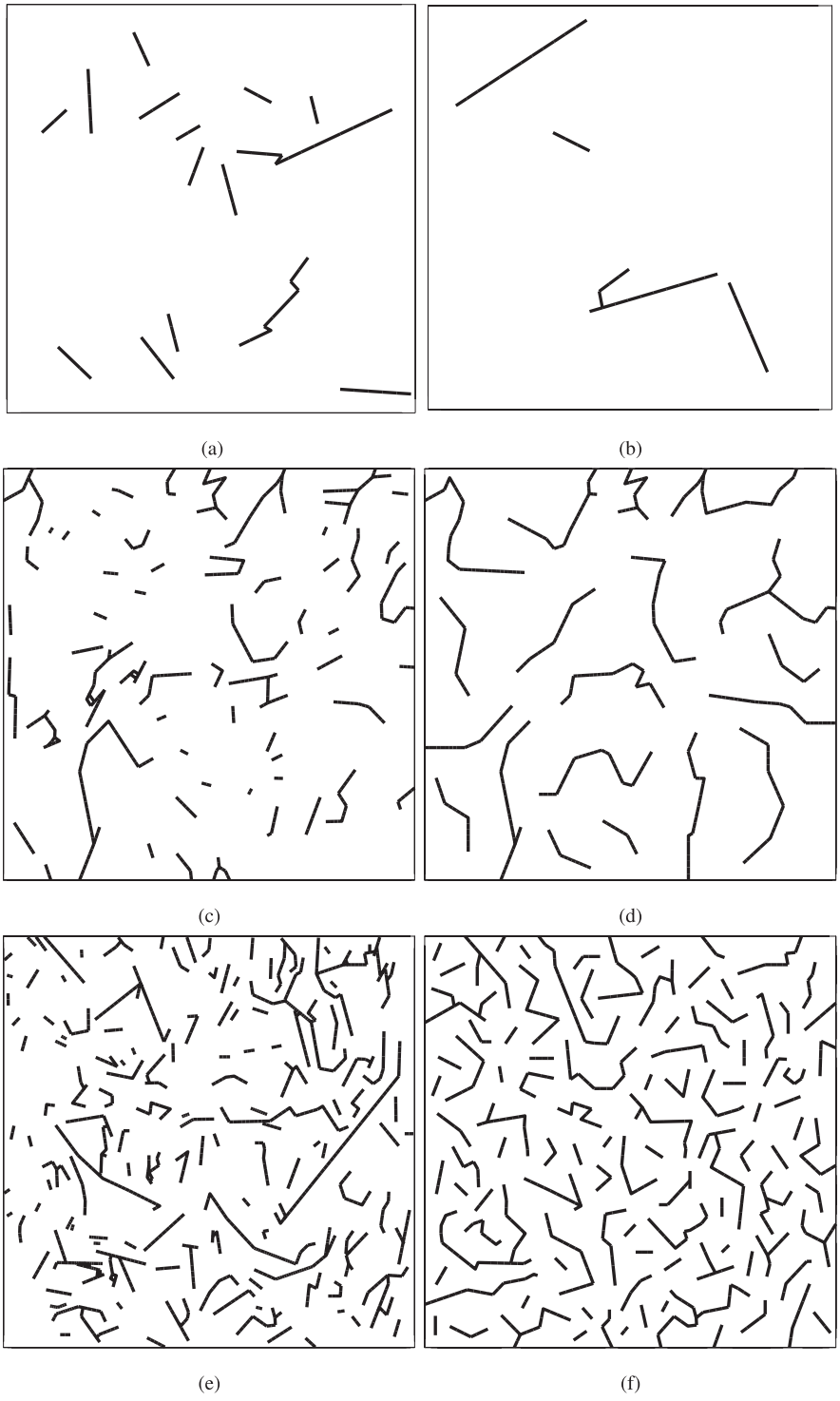

Fig. 8. Resulting image segmentation into matrix and membranes of different regions of the nanocomposite: (a) first material point at 1 wt.%, (b) second material point at 1 wt.%, (c) first material point at 3 wt.%, (d) second material point at 3 wt.%, (e) first material point at 5 wt.%, (f) second material point 5 wt.%.

Table 2
Elastic modulus from experimental test of the GNP-epoxy composites.

Sample	E MPa	Stiffness increase %
GNP 1 wt.%	2941 ± 55	10
GNP 3 wt.%	3193 ± 85	18
GNP 5 wt.%	3366 ± 113	26

The results are collected in Table 2 and are included in Fig. 7 along with the observed scatter. According to [13], the experimental elastic stiffness is increasing, while the tensile strength decreases with increasing weight fraction of the present GNP-filler. It is also noted that the neat epoxy exhibits slightly less brittle behavior compared to that of the GNP-enhanced epoxy.

To study the effect of GNP enhancement on the polymer, two images of each fraction of GNP weight were used to develop the discretized GNP enhanced polymer using the image segmentation described in

Section 2.3. The weight fractions considered are $w^g = 1$, 3, and 5 wt.%. Three discretizations are developed based on the three different weight fractions, resulting in morphologies of the GNP distribution, as shown in Fig. 8. For each weight fraction, two different local material regions presenting different microstructures are considered.

5. Surrogate model identification

To identify the surrogate models, elastic finite element plane strain analyzes are carried out following the sequel (5)–(14). The sample is discretized using standard 2D bilinear elements, and the GNP membranes are embedded along the boundaries between the elements. Our experience is that the details of the mesh design and the size of the RAE are minor for the analysis in the present examples. As mentioned in Section 3.2, the elastic stiffness is obtained from homogenized stresses based on the application of normal macroscopic units and shear strains to the RAE. To relate the homogenized response to the model parameters for the anisotropic elastic response, the least squares fit in (14) was adopted based on a search for each angle $0 \leq \theta \leq 180°$. Fig. 9 shows the resulting microscopic stress distribution for von Mises stress and membrane forces due to the unit shear load considered in computational homogenization. The results are shown for the microstructure in Fig. 8(c) at 3 wt.%. Here, the GNP distribution stiffens the polymer through the membrane stress response of the GNP membranes. As shown in Fig. 9, the Taylor assumption is reflected in the too high membrane forces in the GNPs, corresponding to an overstiff response of the RAE. When the FE-resolved fluctuation field is considered, a more relaxed response is obtained in the GNP-membranes of the RAE. The PBC in Fig. 9 produces a slightly more relaxed RAE compared to the DBC.

Table 3 shows the results of the identified transverse elastic isotropy parameters. In general, an increase in the weight fraction of GNP leads to significant stiffening of the composite. Taking E_2 as a representative parameter, we find that for the lowest weight fraction of GNP, the increase in stiffness (compared to the isotropic neat epoxy parameters in Table 1) is approximately 10%. A greater increase in stiffness is obtained in the biased E_1 direction (20–50%) compared to the increase in the orthogonal 2-direction (up to 10–30%). Taylor's assumption (T), $\boldsymbol{u}^s = \boldsymbol{0}$, is included in Table 3. As expected, unrealistic overstiffening is obtained compared to the more relaxed RAEs. Therefore, the fluctuation field $\boldsymbol{u}^s$ governed by the static momentum balance of the RAE plays an essential role in relaxing the stresses of the RAE.

For comparison, we consider the predicted isotropic elastic response of computational homogenization along the lines set out in Section 3.3. Table 4 shows the parameters identified for all microstructures shown in Fig. 8. In this case, the increase in the weight fraction of GNP yields a stiffness increase of up to $\approx 13-50\%$, depending on the weight fraction. Moreover, this increase is about the same for both the elastic moduli and the shear moduli for all microstructures. As expected, E_{iso} gives an intermediate value between E_1 and E_2 of the transverse isotropic elastic model. Again, it is observed that the sensitivity to the choice of DBC or PBC is minor. Hence, we may conclude that the realizations of the individual microstructures are representative of the elastic properties of the nanocomposite.

6. Halpin–Tsai and Mori–Tanaka models

In order to validate the elastic stiffness predicted by the surrogate models, we follow the developments in [13,19,20] and apply the Halpin–Tsai (HT) equations to the case of randomly distributed GNPs. In the articles, the semi-empirical homogenized elastic stiffness modulus E_{HT} for 3D randomly oriented flakes is composed of a 4/5 contribution from GNPs oriented off-axis to the loading direction and a 1/5 contribution from flakes aligned with the loading direction. The HT

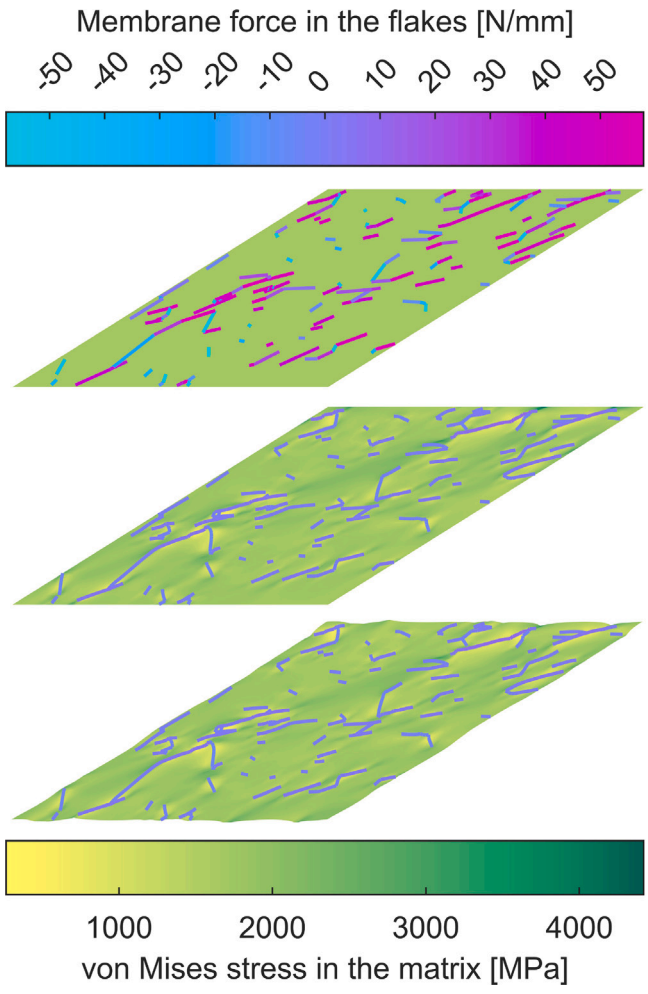

Fig. 9. von Mises stress distribution in polymer and membrane forces N of GNP membranes from FE analysis for a unit shear load applied to the sample at 3 wt.% in Fig. 8(c). Different boundary conditions for the fluctuation field are considered: Taylor assumption (top), Dirichlet boundary conditions for $\boldsymbol{u}^s$ (center), and periodic boundary conditions for $\boldsymbol{u}^s$ (bottom).

stiffness is summarized in terms of matrix stiffness E_m and the standard HT "fiber" stiffening function f, defined as

$$E_{\mathrm{HT}} = E_m\left(\frac{4}{5}f[2] + \frac{1}{5}f[\frac{\xi}{3}]\right) \text{ with } f[\xi] = \frac{1+\xi\eta[\xi]v^g}{1-\eta[\xi]v^g} \text{ and } \eta[\xi] = \frac{E_g/E_m - 1}{E_g/E_m + \xi} \tag{19}$$

where $\xi = 2l_{\mathrm{flake}}/t_{\mathrm{flake}}$ is the length and the thickness of the GNP flakes and v^g is the volume fraction of GNPs considered in (2). In view of the measured lateral flake size and flake thickness in Section 2.1, we estimate $\xi = 2(8.8\times10^{-4})/(5.5\times10^{-6}) = 320$. Moreover, assuming that the GNP-stiffness is isotropic with respect to the longitudinal flake orientation, the ratio E_g/E_m is $876\times10^3/2674 = 328$. Here, it may be observed that $f[\xi\to\infty]$ corresponds to the Voigt bound (or isostrain condition) for GNPs continuous in the loading direction, while $f[\xi\to 0]$ corresponds to the Reuss bound (or isostatic condition) for GNPs continuous transverse to the loading.

We also consider the Mori–Tanaka (MT) method [35], applied to a spherical inclusion in the epoxy matrix. Therefore, GNP flakes are approximated as an embedded GNP sphere in the matrix with volume fraction v^g. The homogenized strain $\bar{\boldsymbol{\epsilon}}$ of the continuum is obtained in terms of the homogenized matrix strain $\boldsymbol{\epsilon}_m$ and the strain in the GNP

Table 3
Identified transverse elastic isotropy parameters from least-squares fits to the computational homogenization for the microstructures depicted in Fig. 8 analyzed based on the Taylor assumption (T), Dirichlet boundary conditions (DBC), and periodic boundary conditions (PBC).

	w^g	Mic.	E_2 (MPa)	G_{23} (MPa)	E_1 (MPa)	G_{12} (MPa)	ν_{12}	θ °
T	1%	8(a)	5309 (99%)	1983 (102%)	5591 (109%)	2320 (136%)	0.33	99.9
		8(b)	4589 (72%)	1625 (65%)	8988 (236%)	1625 (65%)	0.33	62.1
T	3%	8(c)	9139 (242%)	3310 (237%)	15 919 (495%)	4655 (374%)	0.31	28.8
		8(d)	10 606 (297%)	3985 (306%)	14 505 (443%)	4397 (347%)	0.29	18.9
T	5%	8(e)	13 322 (398%)	4820 (390%)	22 815 (753%)	6931 (605%)	0.32	5.4
		8(f)	14 473 (441%)	5340 (443%)	20 445 (664%)	7377 (650%)	0.31	2.7
DBC	1%	8(a)	2973 (11%)	1084 (10%)	3279 (22%)	1084 (10%)	0.35	67.50
		8(b)	2879 (8%)	1033 (5%)	3495 (30%)	1033 (5%)	0.36	61.2
DBC	3%	8(c)	3012 (12%)	1075 (9%)	3715 (39%)	1236 (26%)	0.36	20.7
		8(d)	3371 (26%)	1216 (24%)	3980 (49%)	1315 (34%)	0.35	18.0
DBC	5%	8(e)	3443 (29%)	1238 (26%)	4150 (55%)	1370 (39%)	0.36	10.8
		8(f)	3701 (38%)	1347 (37%)	4187 (57%)	1502 (53%)	0.35	180.0
PBC	1%	8(a)	2953 (11%)	1080 (10%)	3177 (19%)	1080 (10%)	0.35	67.5
		8(b)	2858 (7%)	1030 (5%)	3352 (25%)	1030 (5%)	0.36	62.1
PBC	3%	8(c)	2990 (12%)	1071 (9%)	3590 (34%)	1213 (23%)	0.36	20.7
		8(d)	3324 (24%)	1204 (23%)	3820 (43%)	1285 (31%)	0.35	17.1
PBC	5%	8(e)	3424 (28%)	1236 (26%)	4013 (50%)	1505 (53%)	0.36	4.5
		8(f)	3656 (37%)	1331 (35%)	4141 (55%)	1429 (45%)	0.35	171.0

Table 4
Identified elastic isotropy parameters from least squares fits to the computational homogenization for the microstructures depicted in Fig. 8 analyzed based on the Taylor assumption (T), Dirichlet boundary conditions (DBC), and periodic boundary conditions (PBC).

	w^g	Mic.	E_{iso} (MPa)	G_{iso} (MPa)	ν_{iso}
T	1%	8(a)	5714 (114%)	2165 (120%)	0.32
		8(b)	6346 (137%)	2421 (146%)	0.31
T	3%	8(c)	11 572 (333%)	4497 (358%)	0.29
		8(d)	11 533 (331%)	4481 (356%)	0.29
T	5%	8(e)	17 712 (563%)	6946 (607%)	0.28
		8(f)	18 782 (603%)	7373 (650%)	0.27
DBC	1%	8(a)	3022 (13%)	1118 (14%)	0.35
		8(b)	3122 (17%)	1156 (18%)	0.35
DBC	3%	8(c)	3253 (22%)	1204 (23%)	0.35
		8(d)	3407 (27%)	1259 (28%)	0.35
DBC	5%	8(e)	4118 (54%)	1544 (57%)	0.33
		8(f)	4024 (51%)	1502 (53%)	0.34
PBC	1%	8(a)	3005 (12%)	1111 (13%)	0.35
		8(b)	3033 (13%)	1121 (14%)	0.35
PBC	3%	8(c)	3207 (20%)	1187 (21%)	0.35
		8(d)	3357 (26%)	1241 (26%)	0.35
PBC	5%	8(e)	4011 (50%)	1502 (53%)	0.33
		8(f)	3957 (48%)	1477 (50%)	0.34

inclusion $\boldsymbol{\epsilon}_g$ as

$$\bar{\boldsymbol{\epsilon}} = v^m \boldsymbol{\epsilon}_m + v^g \boldsymbol{\epsilon}_g \text{ with } \boldsymbol{\epsilon}_g = \boldsymbol{A}_g : \boldsymbol{\epsilon}_m \text{ and}$$
$$\boldsymbol{A}_g = \left(\boldsymbol{I} + \boldsymbol{S}_m : \left(\boldsymbol{E}_g : \boldsymbol{E}_m^{-1} - \boldsymbol{I}\right)\right)^{-1} \tag{20}$$

where $\boldsymbol{A}_g$ is the local partitioning tensor obtained from Eshelby's inclusion method [36]. The constitutive stress–strain relations in the constituents are given by

$$\boldsymbol{\sigma}_m = \boldsymbol{E}_m : \boldsymbol{\epsilon}_m \text{ with } \boldsymbol{E}_m = 2G_m \boldsymbol{I}_d + K_m \mathbf{1} \otimes \mathbf{1}$$
$$\boldsymbol{\sigma}_g = \boldsymbol{E}_g : \boldsymbol{\epsilon}_g \text{ with } \boldsymbol{E}_g = 2G_g \boldsymbol{I}_d + K_g \mathbf{1} \otimes \mathbf{1} \tag{21}$$

where $\boldsymbol{E}_m$ and $\boldsymbol{E}_g$ are the isotropic elastic stiffness tensors of the matrix and the GNP particles when confined to the sphere. The homogeneous stress is $\bar{\boldsymbol{\sigma}} = v^m \boldsymbol{\sigma}_m + v^g \boldsymbol{\sigma}_g$, which combined with (20) and (21) yields the homogenized $\boldsymbol{E}_{\mathrm{MT}}$-stiffness as

$$\bar{\boldsymbol{\sigma}} = \boldsymbol{E}_{\mathrm{MT}} : \bar{\boldsymbol{\epsilon}} \rightsquigarrow \boldsymbol{E}_{\mathrm{MT}} = \left(\boldsymbol{E}_m + v^g \left(\boldsymbol{E}_g : \boldsymbol{A}_g - \boldsymbol{E}_m\right)\right) : \left(\boldsymbol{I} + v^g \left(\boldsymbol{A}_g - \boldsymbol{I}\right)\right)^{-1} \tag{22}$$

It appears that MT-homogenized stiffness $\boldsymbol{E}_{\mathrm{MT}}$ is isotropic for the embedded sphere with the Eshelby tensor $\boldsymbol{S}_m = \alpha_1 \boldsymbol{I} + \alpha_2 \mathbf{1} \otimes \mathbf{1}$; the explicit result is

$$\boldsymbol{E}_{\mathrm{MT}} = 2G_{\mathrm{MT}} \boldsymbol{I}_d + K_{\mathrm{MT}} \mathbf{1} \otimes \mathbf{1} \tag{23}$$

where

$$G_{\mathrm{MT}} = G_m \frac{1 + \alpha_1 \left(\frac{G_g}{G_m} - 1\right) + v^g (1 - \alpha_1) \left(\frac{G_g}{G_m} - 1\right)}{1 + \alpha_1 \left(\frac{G_g}{G_m} - 1\right) - v^g \alpha_1 \left(\frac{G_g}{G_m} - 1\right)}$$
$$K_{\mathrm{MT}} = K_m \frac{1 + \alpha_3 \left(\frac{K_g}{K_m} - 1\right) + v^g (1 - \alpha_3) \left(\frac{K_g}{K_m} - 1\right)}{1 + \alpha_3 \left(\frac{K_g}{K_m} - 1\right) - v^g \alpha_3 \left(\frac{K_g}{K_m} - 1\right)} \tag{24}$$

and the coefficients are obtained in terms of the Poisson's ratio ν_m of the matrix defined as

$$\alpha_3 = \alpha_1 + 3\alpha_2 \text{ with } \alpha_1 = \frac{2}{15} \frac{4 - 5\nu_m}{1 - \nu_m} \text{ and } \alpha_2 = \frac{1}{15} \frac{5\nu_m - 1}{1 - \nu_m} \tag{25}$$

For comparison, the isotropic parameters of the MT model are calculated in terms of the homogenized modulus of elasticity E_{MT} and Poisson's ratio ν_{MT} as

$$G_{\mathrm{MT}} = \frac{E_{\mathrm{MT}}}{2(1 + \nu_{\mathrm{MT}})}, \; K_{\mathrm{MT}} = \frac{E_{\mathrm{MT}}}{3(1 - 2\nu_{\mathrm{MT}})} \rightsquigarrow E_{\mathrm{MT}}, \; \nu_{\mathrm{MT}} \tag{26}$$

7. Discussion

In Fig. 10 the parameters of the identified surrogate models considering PBC in Section 5, experimental tensile tests E_{exp} in Table 2 are displayed together to facilitate interpretation. For validation, predictions of the nanocomposite's elastic stiffness based on the HT and MT methods are also included. The morphology of GNPs is considered by applying weights to the HT stiffening function f in (19). In applying the MT model, we limit our focus to the isotropic response of the nanocomposite from (26), considering the GNP filler as an embedded sphere within the matrix with a volume fraction v^g, and not taking into account the two-dimensional morphology of the flakes.

From Fig. 10, surrogate models generally overestimate the stiffness of the nanocomposite, with a higher overprediction for the highest GNP content (5 wt.%). The transverse isotropic surrogate model suggests a variation in stiffness ranging from E_2 to E_1, where the stiffness E_2 is more in line with the tensile tests, while the stiffness E_1 overpredicts the experimental observation. We also note that the stiffness for isotropic behavior, E_{iso} and G_{iso}, takes intermediate values between

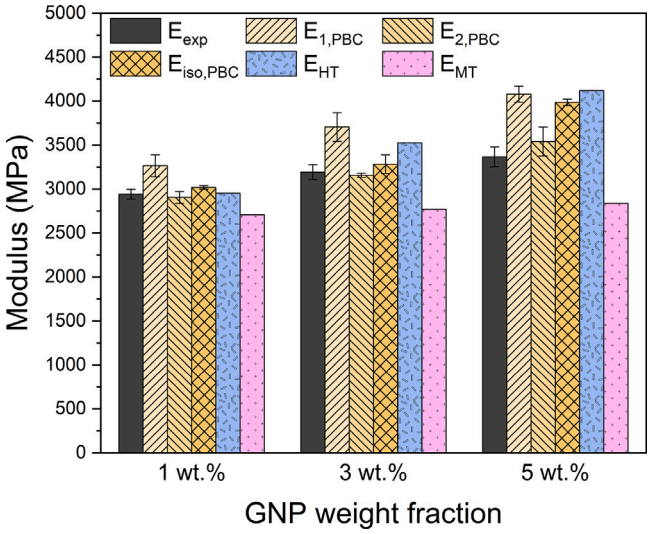

Fig. 10. Comparison between the experimental stiffness (E_{exp}) and the stiffness values obtained with the Halpin–Tsai (E_{HT}), Mori–Tanaka (E_{MT}) and the proposed isotropic ($E_{iso,PBC}$) and anisotropic homogenization method ($E_{1,PBC}$ and $E_{2,PBC}$).

those of the transverse isotropic, $\{E_1, E_2\}$ or $\{G_{12}, G_{23}\}$, for almost all cases. The adopted HT model yields slightly higher estimates of the elastic modulus compared to the surrogate model, thus supporting the results from computational homogenization. However, predictions from the HT model are very sensitive to the adopted weighting of the standard HT fiber stiffening function. The present application of the MT model with the assumption of spherical particles does not account for the GNP morphology. As a result, a lower bound to elastic properties is obtained corresponding to a significant underestimate of stiffness. We also observe the Voigt bound for continuous GNPs transverse to the loading, that is, when the flake aspect ratio ξ approaches infinity. In this case, we obtain the increase in stiffness $f - 1 = \{182\% , 552\% , 928\%\}$ for the volume fractions corresponding to $w^g = \{1\% , 3\% , 5\%\}$, which, as expected, exceed the increases predicted by the Taylor assumption for the RAE in Tables 3 and 4.

The limitations of the homogenization method presented here include the variation of the image throughout the material and the correlation between the 2D and the true 3D properties. The variation in image across the material can be seen by averaging several samples. However, if the nanocomposite has a significant amount of inhomogeneity, then more samples or larger volumes may be required in the homogenization procedure. It is emphasized that the method uses a 2D representation, which artificially creates infinite plate structures (of the 1D GNPs) that run out of plane, possibly leading to overprediction of the stiffness. Furthermore, a perfect bond is assumed between the GNP membranes and the matrix. This also contributes to overstiffening, especially for higher weight fractions, because a larger GNP content increases the surface/length of the interface.

8. Concluding remarks

In this paper, the homogenized macrolevel stiffness of the GNP/polymer microstructure satisfactorily describes the increase in the stiffness of the epoxy matrix as a result of the GNP-reinforcement. To account for the morphology of the graphene platelet network in homogenization, a surface image segmentation analysis of regular SEM micrographs was developed. Detail analysis includes digitization of SEM-visible particles, FE-discretization, and duplication analysis of the morphology to account for the given GNP-weight fraction. The GNPs of the microstructure are modeled as embedded membranes with perfect bonding to the polymer. Here, MD simulations of Hadden et al. [14] on a functionalized layered graphene element were used to estimate the stiffness of the membrane. In computational homogenization, the fluctuation field of momentum balance plays an essential role in describing microstructural relaxation. Both PBC and DBC were considered for the fluctuation field. As expected, the PBC yields a slightly lower estimate of the surrogate stiffness properties. Anisotropic and isotropic elastic surrogate models for microstructural behavior have been identified through least-squares fits of homogenized responses. From the stiffness assessment obtained via the surrogate models, the observed increase in stiffness with respect to the weight fraction of GNPs is verified. From the anisotropic model, there is a "directional" variation in the stiffness, depending on the pointwise morphology of the GNP network. Conservative consideration of the results shows an increase in stiffness of up to 10% to 30% for samples reinforced with 1 to 5 wt.% of GNP, respectively, obtained from the morphological properties and the weight fraction of the carbon content. These findings from the surrogate models are also supported by validation against the HT and MT models. In this context, the anisotropic surrogate reveals a significant local variation in stiffness (even up to 50% increase). Estimates are generally slightly higher than those for experimental tensile testing. This may be explained by ideal perfect GNP bonding to the polymer, the unseen out-of-plane morphology of the GNPs, and local variations in the dispersion state.

CRediT authorship contribution statement

Ragnar Larsson: Supervision, Software, Methodology, Funding acquisition, Formal analysis, Conceptualization. **Danilo J. Carastan:** Validation, Supervision, Funding acquisition, Data curation. **Matheus M. de Oliveira:** Writing – review & editing, Visualization, Validation, Methodology, Data curation. **Linnéa Selegård:** Validation, Funding acquisition. **Mario Martínez:** Writing – review & editing, Visualization, Software, Methodology, Data curation.

Declaration of competing interest

The authors declare that they have no known competing financial interests or personal relationships that could have appeared to influence the work reported in this paper.

Data availability

Data will be made available on request.

Acknowledgments

This work was supported by Vinnova: Multifunctional Composite Structures through Graphene (MULTIGRAPH), Sweden Project number: 2017-02234.

References

[1] A. Ferrari, F. Bonaccorso, V. Fal'ko, K. Novoselov, S. Roche, P. Bøggild, S. Borini, F. Koppens, V. Palermo, N. Pugno, J. Garrido, R. Sordan, A. Bianco, A. Ballerini, M. Prato, E. Lidorikis, Science and technology roadmap for graphene, related two-dimensional crystals and hybrid systems, Nanoscale 7 (2015) 4598–4810.
[2] H. Kim, A. Abdala, C. MacOsko, Graphene/polymer nanocomposites, Macromolecules 43 (16) (2010) 6515–6530.
[3] R. Guzman de Villoria, P. Hallander, L. Ydrefors, P. Nordin, B. Wardle, In-plane strength enhancement of laminated composites via aligned carbon nanotube interlaminar reinforcement, Compos. Sci. Technol. 133 (14) (2016) 33–39.
[4] C. Kostagiannakopoulou, T. Loutas, G. Sotiriadis, A. Markou, V. Kostopoulos, On the interlaminar fracture toughness of carbon fiber composites enhanced with graphene nano-species, Compos. Sci. Technol. 118 (2016) 217–225.
[5] M. Rafiee, J. Rafiee, Z. Wang, H. Song, Z. Yu, N. Koratkar, Enhanced mechanical properties of nanocomposites at low graphene content, ACS Nano 3 (12) (2009) 3884–3890.
[6] A.K. Pathak, M. Borah, A. Gupta, T. Yokozeki, S.R. Dhakatea, Improved mechanical properties of carbon fiber/graphene oxide-epoxy hybrid composites, Compos. Sci. Technol. 135 (27) (2016) 28–38.

[7] L. Tang, Y. Wan, D. Yan, L. Pei, Y. Li, The effect of graphene dispersion on the mechanical properties of graphene/epoxy composites, Carbon 60 (2013) 16–27.
[8] S. Chandrasekaran, N. Sato, F. Tölle, R. Mülhaupt, B. Fiedler, K. Schulte, Fracture toughness and failure mechanism of graphene based epoxy composites, Compos. Sci. Technol. 97 (2014) 90–99.
[9] C. Leopold, W. Liebig, H. Wittich, B. Fiedler, Size effect of graphene nanoparticle modified epoxy matrix, Compos. Sci. Technol. 134 (2016) 217–225.
[10] D. Papageorgiou, I. Kinloch, R. Young, Mechanical properties of graphene and graphene-based nanocomposites, Prog. Mater. Sci. 90 (2017) 75–127.
[11] Z.P. Xiaodong She, L. Kong, Molecular-level dispersion of graphene into epoxidized natural rubber: Morphology, interfacial interaction and mechanical reinforcement, Polymer 61 (2014) 206–214.
[12] S. Prolongo, R. Moriche, A. Jiménez-Suárez, M. Sánchez, A. Ureña, Advantages and disadvantages of the addition of graphene nanoplatelets to epoxy resins, Eur. Polym. J. 61 (2014) 206–214.
[13] J. King, D. Klimek, I. Miskioglu, G. Odegard, Mechanical properties of graphene nanoplatelet/epoxy composites, J. Appl. Polym. Sci. 128 (6) (2013) 4217–4223.
[14] C. Hadden, D. Klimek-McDonald, E. Pineda, J. King, A. Reichanadter, I. Miskioglu, S. Gowtham, G. Odegard, Mechanical properties of graphene nanoplatelet/carbon fiber/epoxy hybrid composites: Multiscale modeling and experiments, Carbon 95 (2015) 100–112.
[15] M. Liu, D. Papageorgiou, S. Li, K. Lin, I. Kinloch, R. Young, Micromechanics of reinforcement of a graphene-based thermoplastic elastomer nanocomposite, Composites A 110 (2018) 84–92.
[16] Q. Meng, Y. Feng, S. Han, F. Yang, M. Demiral, F. Meng, S. Araby, Developing functional epoxy/graphene composites using facile in-situ mechanochemical approach, J. Appl. Polym. Sci. 140 (13) (2023) e53681.
[17] A. Moradi, R. Ansari, M.K. Hassanzadeh-Aghdam, Synergistic effect of carbon nanotube/graphene nanoplatelet hybrids on the elastic and viscoelastic properties of polymer nanocomposites: finite element micromechanical modeling, Acta Mech. 235 (2024) 1887–1909.
[18] M. Haghighi, H. Golestanian, F. Aghadavoudi, Determination of mechanical properties of two-phase and hybrid nanocomposites: experimental determination and multiscale modeling, J. Polym. Eng. 41 (5) (2021) 356–364.
[19] X. Zhao, Q. Zhang, D. Chen, P. Lu, Enhanced mechanical properties of graphene-based poly(vinyl alcohol) composites, Macromolecules 43 (5) (2010) 2357–2363, http://dx.doi.org/10.1021/ma902862u.
[20] T. Zhou, F. Chen, C. Tang, H. Bai, Q. Zhang, H. Deng, Q. Fu, The preparation of high performance and conductive poly (vinyl alcohol)/graphene nanocomposite via reducing graphite oxide with sodium hydrosulfite, Compos. Sci. Technol. 71 (9) (2011) 1266–1270.
[21] J. Guest, I.A. Kinloch, R.J. Young, The role of filler aspect ratio in the reinforcement of an epoxy resin with graphene nanoplatelets, J. Mater. Sci. 58 (2023) 9473–9485, http://dx.doi.org/10.1007/s10853-023-08603-3.
[22] R. Young, M. Liu, I.A.J. Kinloch, S. Li, X. Zhao, C. Vallés, D. Papageorgiou, The mechanics of reinforcement of polymers by graphene nanoplatelets, Compos. Sci. Technol. 154 (18) (2018) 110–116.
[23] M. Liu, D.G. Papageorgiou, S. Li, K. Lin, I.A.J. Kinloch, R. Young, Micromechanics of reinforcement of a graphene-based thermoplastic elastomer nanocomposite, Composites A 110 (2018) 84–92.
[24] B. Blinzler, R. Larsson, K. Gaska, R. Kádár, A mechanics based surface image interpretation method for multifunctional nanocomposites. Nanomaterials, Nanomaterials 9 (2019) 1578, http://dx.doi.org/10.3390/nano9111578.
[25] M. Geers, V. Kouznetsova, W. Brekelmans, Multi-scale computational homogenization: Trends and challenges, J. Comput. Appl. Math. 234 (7) (2010) 2175–2182.
[26] P. Suquet, in: A. Sawczuk, G. Bianchi (Eds.), Local and Global Aspects in the Mathematical Theory of Plasticity, in: Plasticity Today: Modelling, Methods and Applications, Elsevier Applied Science Publishers, London, 1985, pp. 279–310.
[27] F. Larsson, K. Runesson, S. Saroukhani, R. Vafadari, Computational homogenization based on a weak format of micro-periodicity for RVE-problems, Comput. Methods Appl. Mech. Engrg. 200 (2011) 11–26.
[28] A. Javili, P. Steinmann, On thermomechanical solids with boundary structures, Int. J. Solids Struct. 47 (24) (2010) 3245–3253.
[29] R. Auenhammer, N. Jeppesen, L. Mikkelsen, V. Dahl, B. Blinzler, L. Asp, Robust numerical analysis of fibrous composites from X-ray computed tomography image data enabling low resolutions, Compos. Sci. Technol. 224 (16) (2022).
[30] A.K. Kesarwani, O.S. Panwar, S.R. Dhakate, V.N. Singh, R.K. Rakshit, A. Bisht, A. Kumar, Determining the number of layers in graphene films synthesized by filtered cathodic vacuum arc technique, Fullerenes Nanotubes Carbon Nanostruct. 24 (11) (2016) 725–731.
[31] J. Taurozzi, V. Hackley, M. Wiesner, Ultrasonic dispersion of nanoparticles for environmental, health and safety assessment issues and recommendations, Nanotoxicology 5 (2011) 711–729.
[32] M. de Oliveira, S. Forsberg, L. Seleg° ard, D. Carastan, The influence of sonication processing conditions on electrical and mechanical properties of single and hybrid epoxy nanocomposites filled with carbon nanoparticles, Polymers 13 (23) (2021).
[33] R. Larsson, R. Gutkin, M. Rouhi, Damage growth and strain localization in compressive loaded fiber reinforced composites, Mech. Mater. 127 (2018) 77–90.
[34] C. Lee, X. Wei, J. Kysar, J. Hone, Measurement of the elastic properties and intrinsic strength of monolayer graphene, Science 321 (5887) (2008) 385–388.
[35] T. Mori, K. Tanaka, Average stress in matrix and average elastic energy of materials with misfitting inclusions, Acta Metall. 21 (5) (1973) 571–574.
[36] J.D. Eshelby, The determination of the elastic field of an ellipsoidal inclusion, and related problems, Proc. R. Soc. Lond. Ser. A 241 (1226) (1957) 376–396.